POLITECNICO
MILANO 1863

SGN – Assignment #2

Alessandro Massini, 243670

Exercise 1: Uncertainty propagation

You are asked to analyze the state uncertainty evolution along a transfer trajectory in the Planar Bicircular Restricted Four-Body Problem, obtained as optimal solution of the problem stated in Section 3.1 (Topputo, 2013)[*]. The mean initial state $\mathbf{x}_i$ at initial time t_i with its associated covariance $\mathbf{P}_0$ and final time t_f for this optimal transfer are provided in Table 1.

1. Propagate the initial mean and covariance within a time grid of 5 equally spaced elements going from t_i to t_f, using both a Linearized Approach (LinCov) and the Unscented Transform (UT). We suggest to use $\alpha = 1$ and $\beta = 2$ for tuning the UT in this case. Plot the mean and the ellipses associated with the position elements of the covariances obtained with the two methods at the final time.

2. Perform the same uncertainty propagation process on the same time grid using a Monte Carlo (MC) simulation [†]. Compute the sample mean and sample covariance and compare them with the estimates obtained at Point 1). Provide the following outputs.

   - Plot of the propagated samples of the MC simulation, together with the mean and the covariance obtained with all methods in terms of ellipses associated with the position elements at the final time.
   - Plot of the time evolution (for the time grid previously defined) for all three approaches (MC, LinCov, and UT) of $3\sqrt{\max_i(\lambda_i(P_r))}$ and $3\sqrt{\max_i(\lambda_i(P_v))}$, where P_r and P_v are the 2x2 position and velocity covariance submatrices.
   - Plot resulting from the use of the MATLAB function `qqplot`, for each component of the previously generated MC samples at the final time.

Compare the results, in terms of accuracy and precision, and discuss on the validity of the linear and Gaussian assumption for uncertainty propagation.

Table 1: Solution for an Earth-Moon transfer in the rotating frame.

Parameter	Value
Initial state $\mathbf{x}_i$	$\mathbf{r}_i = [\text{-0.011965533749906, -0.017025663128129}]$
	$\mathbf{v}_i = [10.718855256727338, 0.116502348513671]$
Initial time t_i	1.282800225339865
Final time t_f	9.595124551366348
Covariance $\mathbf{P}_0$	$\begin{bmatrix} +1.041e-15 & +6.026e-17 & +5.647e-16 & +4.577e-15 \\ +6.026e-17 & +4.287e-18 & +4.312e-17 & +1.855e-16 \\ +5.647e-16 & +4.312e-17 & +4.432e-16 & +1.455e-15 \\ +4.577e-15 & +1.855e-16 & +1.455e-15 & +2.822e-14 \end{bmatrix}$

1.1 LinCov and UT Uncertainty Propagation

The analysis of the state uncertainty evolution was conducted, starting from the data in Table 1, exploiting two different approaches: the Linearized Approach (LinCov) which relies on linearization assumptions, and Unscented Transform (UT) aiming to better represent the final Probability Density Function (PDF).

In the LinCov methodology, it is assumed that the linearized dynamics provides a sufficiently accurate representation of the perturbed trajectory. To estimate the mean and covariance along the trajectory, the initial state ($\mathbf{x_0}$) is propagated using a numerical Planar Bicircular Restricted Four-Body Problem (PBR4BP) integrator over a discretized time grid consisting of five points between t_i to t_f. At each point on the grid, the State Transition Matrix ($\mathbf{\Phi}(t_0, t_k)$), with k the $k - th$ point on the time grid, is computed using a variational approach. The final mean and covariance are then determined as:

$$\hat{\mathbf{x}}_{\mathbf{LinCov}} = \boldsymbol{\varphi}(\mathbf{x_0}, t_0, t_f) \quad \mathbf{P}(t_f) = \mathbf{\Phi}(t_0, t_f)\mathbf{P_0}\mathbf{\Phi}(t_0, t_f)^T \tag{1}$$

It is important to highlight that this approach, which relies on linearization, provides an acceptable approximation of the true state only when the nonlinearity of the dynamics is relatively low.

As the linear methods could fail on estimating the correct final mean and covariance, a comparison with the UT method is perfomed. The idea behind the UT method is to parametrize the inital PDF with a small number of samples correcting representing the inital mean and covariance, to propagate them over the aforementioned time grid with the PBR4BP propagator and, finally, to estimate the final mean and covariance exploiting weighted sample mean and covariance. Defining $\boldsymbol{\chi_i}$ the initial samples and $\boldsymbol{\gamma_i} = \boldsymbol{\varphi}(\boldsymbol{\chi_i}, t_0, t_f)$ the final ones, $\hat{\mathbf{x}}_{\mathbf{UT}}$ and $\mathbf{P_{UT}}$ are obtained as:

$$\hat{\mathbf{x}}_{\mathbf{UT}} = \sum_{i=0}^{2n} W_i \boldsymbol{\gamma_i} \qquad \mathbf{P_{UT}} = \sum_{i=0}^{2n} W_i \left(\boldsymbol{\gamma_i} - \hat{\mathbf{x}}_{\mathbf{UT}}\right)\left(\boldsymbol{\gamma_i} - \hat{\mathbf{x}}_{\mathbf{UT}}\right)^T \tag{2}$$

The UT approach is more appropriate for representing the system's inherent non-linearities as it does not require linearizations. In addition, it can also approximate non-Gaussian distributions, which are characteritics of long term propagations.

In Fig. 1 is showcased the output of the two different propagations in terms of Mean Position and Covariance Ellipse in the Rotating Reference Frame.
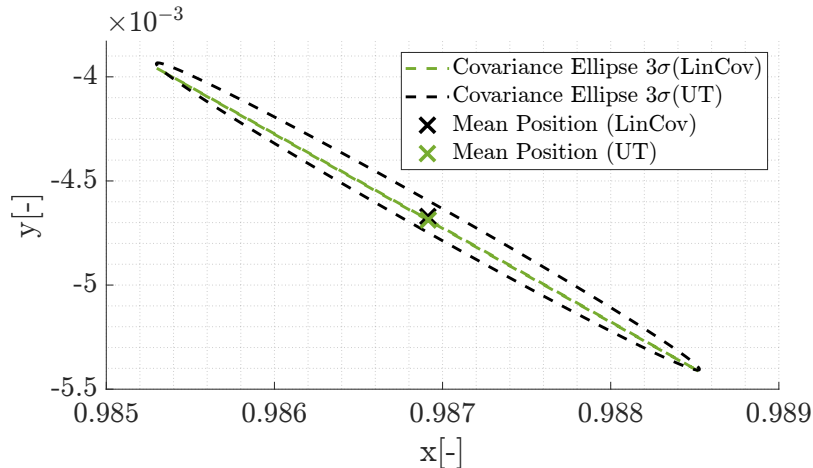

Figure 1: Comparison between LinCov and UT methods

1.2   Monte Carlo Simulation

The same uncertainty propagation was performed through a Monte Carlo (MC) simulation. The sample size was set to $n = 1000$ to ensure computational efficiency. The Gaussian distribution of the population was enforced exploiting the MATLAB function `mvnrnd` and then, each generated element, was propagated with the same strategy described in Section 1.1. In the end, final mean and covariance are estimated through:

$$\hat{\mathbf{x}}_{\mathbf{MC}} = \frac{1}{n} \sum_{i=1}^{n} \mathbf{x_i} \qquad \mathbf{P}_{\mathbf{MC}} = \frac{1}{n-1} \sum_{i=1}^{n} \left(\mathbf{x_i} - \hat{\mathbf{x}}_{\mathbf{MC}} \right) \left(\mathbf{x_i} - \hat{\mathbf{x}}_{\mathbf{MC}} \right)^T \tag{3}$$

with $\mathbf{x_i}$ is the state of the $i - th$ element of the simulation.

In Fig. 2 is showcased the output of the MC simulation compared with the two method previously analyzed.
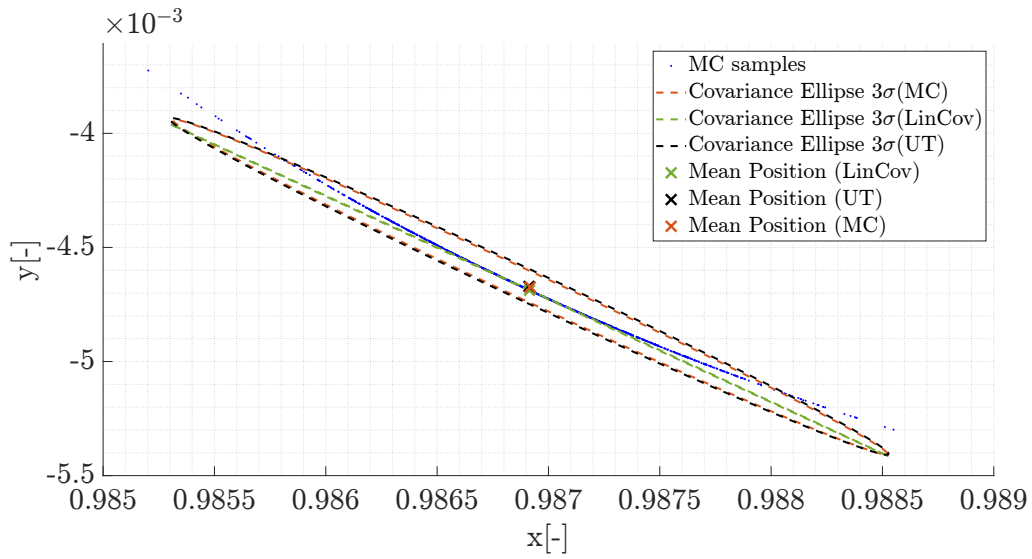

Figure 2: Comparison between LinCov, UT and MC methods

It is clear from the distribution of the MC samples that the LinCov method is capable to effectively capture only the displacement along the primary direction of propagation. The rationale behind the flattening shape of the LinCov ellipse lies in the reliance on linearization; over this strong assumption the LinCov covariance underestimates the spread of uncertaintes in secondary directions over long propagation time or in the presence of significant non-linearities. Conversely, UT and MC covariance ellipse demonstrate to more accurately represent the behavior of the majority of the propagated elements. Taking the MC methods as a criterion due to its statistical sampling nature, the UT methods closely match its reference both in terms of Mean Position and Covariance, demonstrating the validity of the approach in capturing the non-linearities of the system, under the given assumptions.
In terms of Mean Position the three methods don't differ substantially even if the LinCov one exhibits a slight deviation with respect to MC and UT which are almost overlapped.

Overall, Fig. 2 shows how, in the given dynamics and propagation interval, the LinCov method fails in fully capture the uncertainties while still offering a valid approximation for the Mean Position. The MC method, on the contrary, represents the reference statistical result and therefore inherently captures the true uncertainties distribution, although it requires significant computational resources. Finally, the UT method appears as the best compromise for both accuracy and efficiency as, the parametrization of the initial PDF with a small number of carefully chosen sigma points allows to capture the uncertainties propagation the propagation of uncertainties while maintaining computational performance.

In Fig. 3 is shown the time evolution of the maximum Eigenvalue of the Covariance sub matrices for both position and velocity. In the early phases of the propagation, the uncertainties remain almost constant showcasing a stable behavior across all the three methods. However, in the last interval a strong increase of the uncertainties can be observed suggesting that all the three methods are influenced by the non-linearities of the system dynamics.

The near-perfect overlap of the LinCov method with the UT and MC results serves as evidence that linearized methods can effectively track uncertainties along the primary direction of propagation.
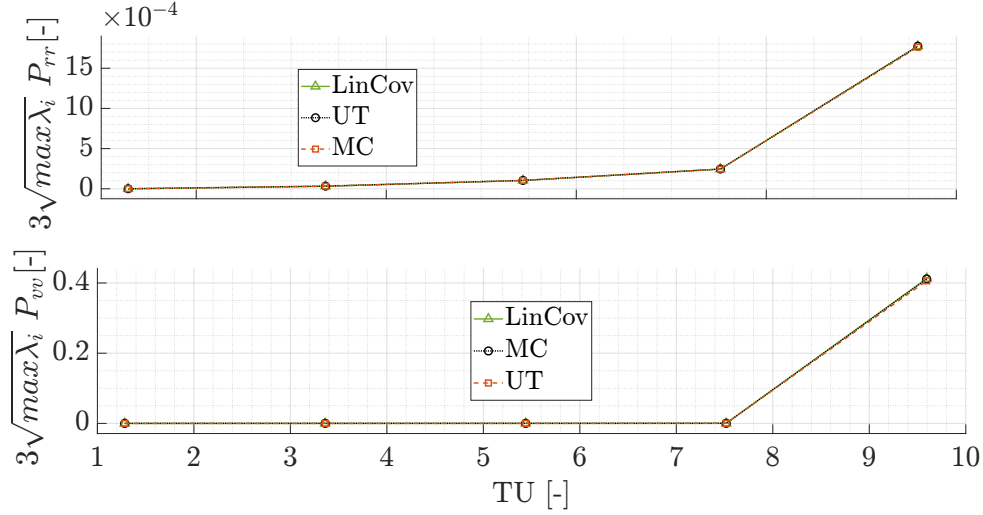

Figure 3: Comparison of square root of the maximum Eigenvalue evolution for Position and Velocity Covariance submatrices using LinCov, UT, and MC methods.

In order to validate the results, in Fig. 4 are shown the QQ-plots of the MC samples for each state component. The distributions of x, y and v_y exhibit a strong alignment with the Gaussianity assumption, as the empirical quantiles closely follow the theoretical normal quantiles across the entire range. However, the plot v_x assume a characteristic 'U-Shape'. This behavior indicates that the samples for this component have a higher frequency of extreme values, which is probably due to non-linear effects in the system dynamics.
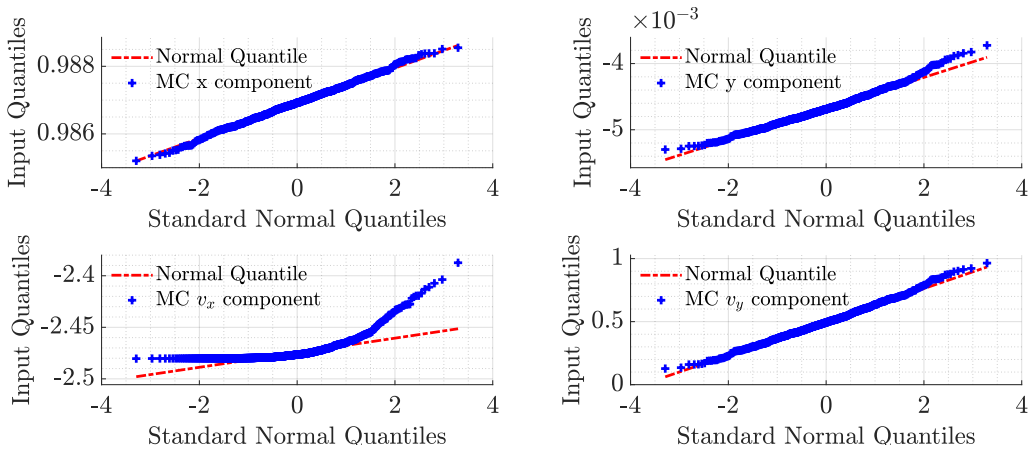

Figure 4: QQ-plots for each state component at the final time

In conclusion, the analysis has shown that, as time progresses, uncertainty propagation introduces deviations from the Gaussian distribution. However, these deviations remain within a range in which the UT method accurately captures the overall behavior, while the LinCov provides acceptable results limited to the principal direction of propagation.

POLITECNICO
MILANO 1863

Exercise 2: Batch filters

The Soil Moisture and Ocean Salinity (SMOS) mission, launched on 2 November 2009, is one of the European Space Agency's Earth Explorer missions, which form the science and research element of the Living Planet Programme.

You have been asked to track SMOS to improve the accuracy of its state estimate. To this aim, you shall schedule the observations from the three ground stations reported in Table 2.

1. *Compute visibility windows.* The Two-Line Elements (TLE) set of SMOS are reported in Table 3 (and in WeBeep as 36036.3le). Compute the osculating state from the TLE at the reference epoch t_{ref}, then propagate this state assuming Keplerian motion to predict the trajectory of the satellite and compute all the visibility time windows from the available stations in the time interval from t_0 = 2024-11-18T20:30:00.000 (UTC) to t_f = 2024-11-18T22:15:00.000 (UTC). Consider the different time grid for each station depending on the frequency of measurement acquisition. Report the resulting visibility windows and plot the predicted Azimuth and Elevation profiles within these time intervals.

2. *Simulate measurements.* Use SGP4 and the provided TLE to simulate the measurements acquired by the sensor network in Table 2 by:

   (a) Computing the spacecraft position over the visibility windows identified in Point 1 and deriving the associated expected measurements.

   (b) Simulating the measurements by adding a random error to the expected measurements (assume a Gaussian model to generate the random error, with noise provided in Table 2). Discard any measurements (i.e., after applying the noise) that does not fulfill the visibility condition for the considered station.

3. *Solve the navigation problem.* Using the measurements simulated at the previous point:

   (a) Find the least squares (minimum variance) solution to the navigation problem without a priori information using

   - the epoch t_0 as reference epoch;
   - the reference state as the state derived from the TLE set in Table 3 at the reference epoch;
   - the simulated measurements obtained for the KOROU ground station only;
   - pure Keplerian motion to model the spacecraft dynamics.

   (b) Repeat step 3a by using all simulated measurements from the three ground stations.

   (c) Repeat step 3b by using a J2-perturbed motion to model the spacecraft dynamics.

   Provide the results in terms of navigation solution[‡], square root of the trace of the estimated covariance submatrix of the position elements, square root of the trace of the estimated covariance submatrix of the velocity elements. Finally, considering a linear mapping of the estimated covariance from Cartesian state to Keplerian elements, provide the standard deviation associated to the semimajor axis, and the standard deviation associated to the inclination. Elaborate on the results, comparing the different solutions.

4. *Trade-off analysis.* For specific mission requirements, you are constrained to get a navigation solution within the time interval reported in Point 1. Since the allocation of antenna time has a cost, you are asked to select the passes relying on a budget of 70.000 €. The cost per pass of each ground station is reported in Table 2. Considering this constraint,

---

[‡]Not just estimated state or covariance

and by using a J2-perturbed motion for your estimation operations, select the best combination of ground stations and passes to track SMOS in terms of resulting standard deviation on semimajor axis and inclination, and elaborate on the results.

5. *Long-term analysis.* Consider a nominal operations scenario (i.e., you are not constrained to provide a navigation solution within a limited amount of time). In this context, or for long-term planning in general, you could still acquire measurements from multiple locations but you are tasked to select a set of prime and backup ground stations. For planning purposes, it is important to have regular passes as this simplifies passes scheduling activities. Considering the need to have *reliable* orbit determination and *repeatable* passes, discuss your choices and compare them with the results of Point 4.

Table 2: Sensor network to track SMOS: list of stations, including their features.

Station name	KOUROU	TROLL	SVALBARD
Coordinates	LAT = 5.25144° LON = -52.80466° ALT = -14.67 m	LAT = -72.011977° LON = 2.536103° ALT = 1298 m	LAT = 78.229772° LON = 15.407786° ALT = 458 m
Type	Radar (monostatic)	Radar (monostatic)	Radar (monostatic)
Measurements type	Az, El [deg] Range (one-way) [km]	Az, El [deg] Range (one-way) [km]	Az, El [deg] Range (one-way) [km]
Measurements noise (diagonal noise matrix R)	$\sigma_{Az,El} = 125$ mdeg $\sigma_{range} = 0.01$ km	$\sigma_{Az,El} = 125$ mdeg $\sigma_{range} = 0.01$ km	$\sigma_{Az,El} = 125$ mdeg $\sigma_{range} = 0.01$ km
Minimum elevation	6 deg	0 deg	8 deg
Measurement frequency	60 s	30 s	60 s
Cost per pass	30.000 €	35.000 €	35.000 €

Table 3: TLE of SMOS.

```
1 36036U 09059A   24323.76060260  .00000600  00000-0  20543-3 0  9995
2 36036  98.4396 148.4689 0001262  95.1025 265.0307 14.39727995790658
```

2.1 Visibility Windows

The objective of the first point of Exercise 2 is to compute the visibility windows of SMOS from three Ground Stations (GS), respectively, Kourou, Troll, and Svalbard. The visibility window is defined as the time interval during which the satellite remains observable from a given station and, therefore, during which the satellite's elevation angle, as measured from the station, exceeds the station-specific minimum elevation threshold.

The computation started with the provided TLE of the satellite, which served as the initial data source. The reference epoch (t_{ref}) and the reference state vector in ECI ($\mathbf{x_{ref}}$, see Table 4.) were both recovered using SGP4 algorithm. Given that the observation period spans from t_0 to t_f, the satellite's state was propagated from the reference epoch to t_0 using a Keplerian propagator, enabling the determination of the initial state vector for the subsequent analysis.

| Position $[x, y, z]$ [km]	$[-6065.4138, 3768.0469, 14.5009]$
Velocity $[v_x, v_y, v_z]$ [km/s]	$[0.6036, 0.9267, 7.3908]$

**Table 4:** SMOS' Cartesian State at t_{ref}(@Earth ECI reference frame).

The trajectory of the satellite is then propagated throughout the time window, with the time step determined according to the minimum measurement frequency specific to each station (Table 2). In order to retrieve Range, Azimuth and Elevation using the SPICE function `cspice_xfmsta`, the relative states between SMOS and the stations in ECI were computed exploiting `cspice_spkezr` and then rotated in the stations' TOPOCENTRIC reference frame through `cspice_sxform`. Finally, the visibility windows corresponding to each station were retrived; the results are provided in Table 5 in terms of UTC start and end time, along with the total number of satellite acquisitions provided by each station.

Table 5: Visibility windows for SMOS tracking.

Station	Start Time (UTC)	End Time (UTC)	Number of Acquisitions
Kourou	2024-11-18T20:40:00.000	2024-11-18T20:49:00.000	10
Troll	2024-11-18T21:02:30.000	2024-11-18T21:11:30.000	19
Svalbard	2024-11-18T21:56:00.000	2024-11-18T22:06:00.000	11

The following figures (Fig. 5, 6, 7) display the satellite's Azimuth and Elevation as functions of time in the graph on the left. The graph on the right complements this information by illustrating the relationship between Azimuth and Elevation, offering a comprehensive view of the satellite's visibility geometry with respect to the ground stations. Together, these plots facilitate an in-depth understanding of the satellite's trajectory and its visibility dynamics across the defined time window.
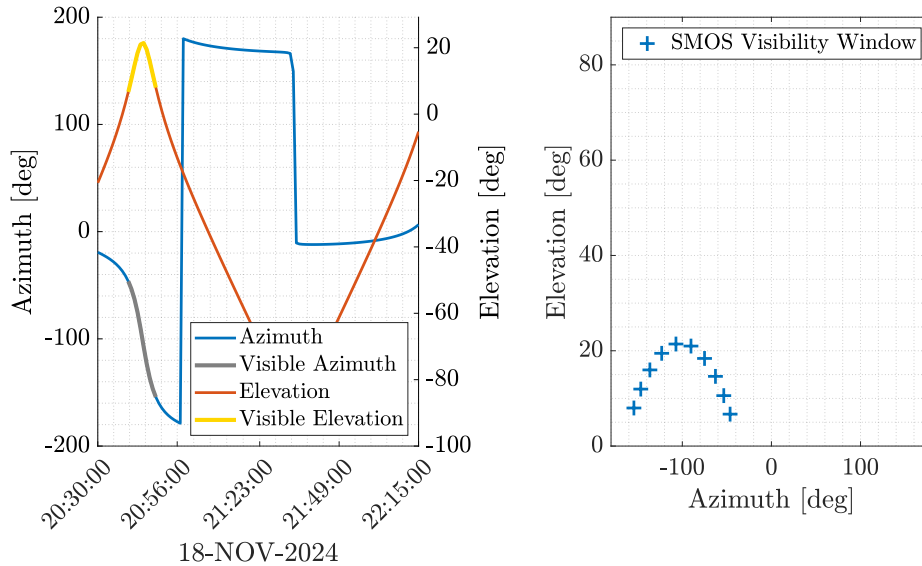
Figure 5: SMOS pass from KOUROU station
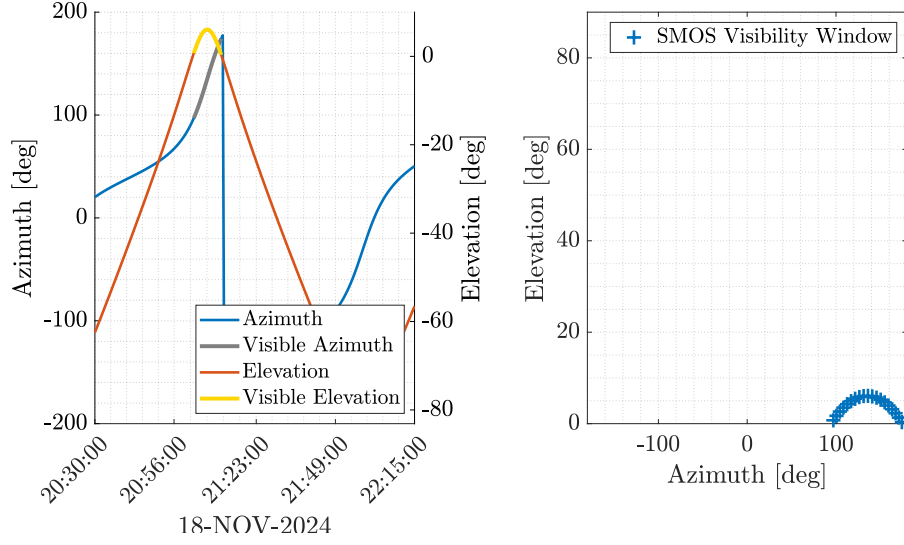
Figure 6: SMOS pass from TROLL station
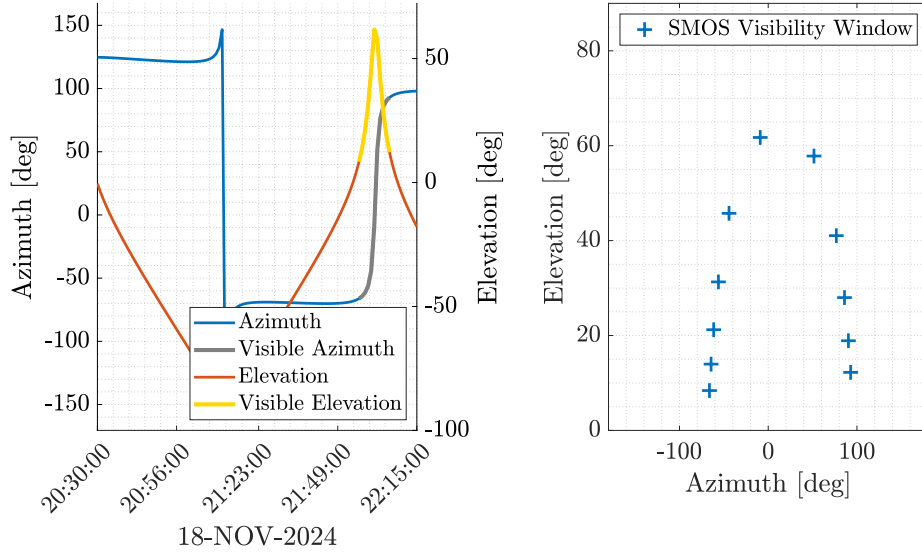
Figure 7: SMOS pass from SVALBARD station

2.2 Measurements Simulation

The aim of the Exercise 2.2 is to simulate the real measurements of the satellite provided by the stations. To achieve this, the trajectory was from t_0 to t_{ref} using `SGP4` algorithm. This method is able to provide a more accurate state estimate compared to the Keplerian propagator, as it accounts for perturbative effects such as Earth's oblateness (J2) and atmospheric drag, which significantly influence the satellite's motion in low Earth orbit. The strategy followed to retrieve Range, Azimuth and Elevation for each station is the same proposed in the previous section. The shift between the measurements computed with the Keplerian Propagator and those obtainted with `SGP4` is shown in Fig. 8.

Furthermore, to better simulate real-world scenarios, random noise was added through the MATLAB function `mvnrnd`. The noise was generated based on the noise covariance matrix specified in Table 2, ensuring the measurements reflect realistic observation uncertainties. After adding the noise, the measurements were rechecked against the visibility windows to ensure they remained within the defined observable conditions.
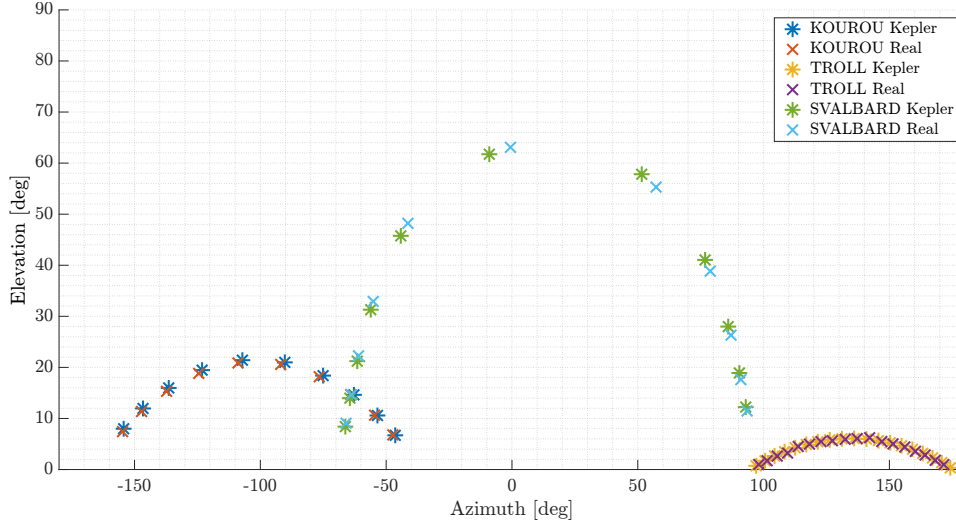
Figure 8: Measurements from Stations: Keplerian Propagation vs `SGP4`(with Noise).

2.3   Navigation Problem

This section focuses on the resolution of the Navigation Problem in three different scenarios. The first analysis was conducted considering only the measurements from Kourou Station, while in the second scenario data from all the stations were utilized. Finally, in the third condition, the J2 perturbation was incorporated into the Keplerian propagator to achieve a solution that more accurately reflects real-world conditions.

The problem was solved exploiting a least-squares optimization implemented through the MATLAB function `lsqnonlin`. Particularly, the `levemberg-marquardt` algorithm was employed as it is specifically well-suited when the initial guess of the optimization is distant from the optimal. The general formulation of the problem, defining $\mathbf{r_{ij}}$ the residuals vector and $\mathbf{W_i}$ the weighting matrix, is:

$$\text{find } \min_{\mathbf{x_0}} \sum_{j=1}^{N_S} \sum_{i=1}^{N_m} \mathbf{W_i r_{ij}} \tag{4}$$

where N_S is the number of ground stations considered into the specific optimization and N_m is the number of measurements for a specific station. The residual vector is defined as the difference between the real measurements simulated in Section 2.2 and the measurements obtained by propagating the optimization variables, following the same methodology outlined in Section 2.1. The weighting matrix, on the other hand, reflects the confidence assigned to each measurement and it is derived from the standard deviations specified in Table 2.

The solution is provided in terms of optimal Mean State and Covariance along with the traces of the Position and Velocity submatrices. Additionally, the standard deviations for the orbit semi-major axis and inclination are also derived by applying a linear transformation from the state covariance matrix to the Keplerian elements one. For this purpose, once the solver determined the optimal initial mean state and the associated covariance, these were utilized to compute the nominal Keplerian elements and the corresponding Jacobian matrix. The Jacobian was retrieved with respect to variations in the state components using a Forward Finite Differences method. Then the covariance matrix of the Keplerian Element was obtained as:

$$\mathbf{P}_{kepler} = \mathbf{J} \mathbf{P}_{state} \mathbf{J}^{\mathrm{T}} \tag{5}$$

where $\mathbf{P}_{state}$ denotes the state-space covariance matrix, and $\mathbf{J}$ is the Jacobian matrix representing the linear transformation of uncertainties from the state-space to the Keplerian elements domain. The results of the three analyses are outlined in Table 6:

Table 6: Navigation Solutions at time t_0 (@Earth ECI frame), Matrix Units: $\left[km, \dfrac{km^2}{s} \right]$

(a) Kourou Measurements only

Position in ECI $[x, y, z]$ [km]	[3932.7931, -1415.5298, 5780.2312]
Velocity in ECI $[v_x, v_y, v_z]$ [km/s]	[4.8841, -3.7626, -4.2373]
$\boldsymbol{\sigma_{rr}}$ **[km]**	9.3806
$\boldsymbol{\sigma_{vv}}$ **[km/s]**	0.0109
$\boldsymbol{\sigma_a}$ **[km]**	7.2624
$\boldsymbol{\sigma_i}$ **[deg]**	0.0696

$$
\mathbf{P_0} = \begin{bmatrix}
57.2769 & 6.2184 & 0.2988 & -0.0615 & -0.0230 & -0.0367 \\
6.2184 & 23.8513 & -12.3562 & 6.7882e-4 & -0.0191 & 0.0053 \\
0.2988 & -12.3562 & 6.8673 & -0.0042 & 0.0083 & -0.0054 \\
-0.0615 & 6.7882e-4 & -0.0042 & 6.8309e-5 & 1.9306e-5 & 4.2260e-5 \\
-0.0230 & -0.0191 & 0.0083 & 1.9306e-5 & 2.2313e-5 & 8.5871e-6 \\
-0.0367 & 0.0053 & -0.0054 & 4.2260e-5 & 8.5871e-6 & 2.7464e-5
\end{bmatrix}
$$

(b) Measurements from all Ground Stations

Position in ECI $[x, y, z]$ [km]	[3926.7744, -1410.9255, 5780.0699]
Velocity in ECI $[v_x, v_y, v_z]$ [km/s]	[4.8887, -3.7650, -4.2333]
$\boldsymbol{\sigma_{rr}}$ **[km]**	1.0227
$\boldsymbol{\sigma_{vv}}$ **[km/s]**	0.0010
$\boldsymbol{\sigma_a}$ **[km]**	0.1485
$\boldsymbol{\sigma_i}$ **[deg]**	0.0020

$$
\mathbf{P_0} = \begin{bmatrix}
0.5963 & -0.3718 & -0.0920 & -5.9982e-4 & 2.0137e-4 & -3.6505e-4 \\
-0.3718 & 0.3736 & 0.0866 & 4.3045e-4 & -1.0175e-4 & 2.7510e-4 \\
-0.0920 & 0.0866 & 0.0760 & 6.5000e-5 & -2.3462e-5 & 9.3825e-5 \\
-5.9982e-4 & 4.3045e-4 & 6.5000e-5 & 6.8693e-7 & -1.6847e-7 & 3.7192e-7 \\
2.0137e-4 & -1.0175e-4 & -2.3462e-5 & -1.6847e-7 & 1.1321e-7 & -1.1966e-7 \\
-3.6505e-4 & 2.7510e-4 & 9.3825e-5 & 3.7192e-7 & -1.1966e-7 & 2.6811e-7
\end{bmatrix}
$$

(c) Measurements from all Ground Stations and J2-Perturbed Dynamics

Position in ECI $[x, y, z]$ [km]	[3932.7876, -1414.9280, 5778.4991]
Velocity in ECI $[v_x, v_y, v_z]$ [km/s]	[4.8789, -3.7632, -4.2329]
$\boldsymbol{\sigma_{rr}}$ **[km]**	0.0264
$\boldsymbol{\sigma_{vv}}$ **[km/s]**	0.000021636
$\boldsymbol{\sigma_a}$ **[km]**	0.0061
$\boldsymbol{\sigma_i}$ **[deg]**	0.000068818

$$
\mathbf{P_0} = \begin{bmatrix}
2.9496e-4 & -2.2831e-4 & -3.9024e-5 & -2.6949e-7 & 1.0277e-7 & -1.5717e-7 \\
-2.2831e-4 & 3.6021e-4 & 5.1697e-5 & 2.4697e-7 & -5.7942e-8 & 1.5118e-7 \\
-3.9024e-5 & 5.1697e-5 & 4.4316e-5 & 1.0803e-8 & -1.0289e-8 & 4.2696e-8 \\
-2.6949e-7 & 2.4697e-7 & 1.0803e-8 & 2.9521e-10 & -7.2765e-11 & 1.4025e-10 \\
1.0277e-7 & -5.7942e-8 & -1.0289e-8 & -7.2765e-11 & 6.5286e-11 & -5.4421e-11 \\
-1.5717e-7 & 1.5118e-7 & 4.2696e-8 & 1.4025e-10 & -5.4421e-11 & 1.0764e-10
\end{bmatrix}
$$

The results summarized in Table 6 provide a comprehensive comparison of the Navigations solutions obtained under different operative conditions. As expected, the worst performance is observed in the case where only Kourou is considered as observer. The reason is to be attribute to the limited number of observations combined with the geometric limitations that are inherently presents when a single station provides measurements. Indeed, a single ground station can effectively estimate only the state components influencing range, azimuth, and elevation directly, and closely aligning with the line-of-sight direction. Components orthogonal to it, such as cross-track position and velocity, remain poorly constrained, leading to larger estimation errors.

When using all the three GS, several critical improvements occur, enhancing fundamentally the state estimation accuracy and reliability. Firstly, having measurements from multiple independent sources enables cross-validation, making the solution more robust and less susceptible to noise or biases originating from any single station. This redundancy ensures that errors in individual measurements have a reduced impact on the final state estimation. Secondly, the diverse geographic positions of the three stations provide observations from three distinct lines of sight, improving drastically system's sensitivity to all state components. This enhanced geometric diversity resolves ambiguities, particularly for components orthogonal to the line-of-sight, which are constraint poorly with a single station observation. Finally, the near-continuous temporal coverage offered by the three stations minimizes reliance on orbital propagation to fill gaps between observations. This consistency ensures a more realistic and constraint solution leading to a better estimate of the satellite's initial state and the consequent trajectory. Together, these factors underscore the critical importance of multi-station setups for robust and high-precision orbit determination.

The final significant improvement in the navigation solution stems from the incorporation of the J2 perturbation into the Keplerian propagator. Accounting for this perturbative effect enables the propagator to become more consistent with the dynamics modeled by the SGP4 algorithm, as it takes into consideration orbital phenomena such as nodal regression or perigee precession. Consequently, can be identified a further decrease in the discrepancies between the propagated trajectory and the measurements, resulting in a navigation solution that manage to achieve the highest accuracy in the state estimation and the most significant uncertainties reduction.

2.4 Trade-Off Analysis

Following the simulation of a scenario with no budget constraints, where all ground stations are available for orbit determination, the analysis gradually moves towards to a nominal operational scenario. The first step was a trade-off analysis over the time interval specified in Table 2, with a budget of 70,000€. The goal was to choose the best combination of ground stations to minimize the standard deviations of the semi-major axis and inclination.

The dynamic was modeled including the J2 effect into the propagator and, due to the aforementioned budget constraint, the evaluation was executed considering only two stations providing measurements. The procedure follows the methodology outlined in Section 2.3. The outcomes of the three possible combinations are summarized in Table 7 in terms of standard deviation of semi-major axis and inclination:

Table 7: Trade-off analysis results

	Kourou-Troll	Kourou-Svalbard	Troll-Svalbard
$\boldsymbol{\sigma}_a[km]$	0.75681	0.01241	0.04892
$\boldsymbol{\sigma}_i$ [deg]	0.00178	4.5132e-04	6.54702e-04

The outcomes of the analysis highlight certain differences among the three possible scenarios. As highlighted in Section 2.3, the accuracy of the state estimation is largely dependent on the spatial coverage offered by the chosen ground stations. Achieving reliable and accurate estimations requires the availability of several measurement types from geographically dispersed stations at different latitudes, particularly in light of SMOS' polar orbit.

The same importance is given to the temporal distribution of the considered measurements: a well distributed set of observation allows the filter to correct the errors coming from the uncostraint propagation.

In light of these considerations, the results shown in Table 6 can be easily validated. The Kourou-Svalbard scenario emerges as the best combination in minimizing both semi-major axis and inclination uncertainties. Indeed, this combination offer a comprehensive spatial coverage: Kourou, located near the equator (LAT = 5.25°), is able to provide low-latitude measurements which are highly sensitive to semi-major axis variations, while Svalbard, positioned almost at the north pole (LAT = 78.23°), furnishes polar observations that enhance significantly inclination estimate. Furthermore, the temporal distribution of the two visibility windows in the specified time interval significantly enhances the quality the solution. In fact, Kourou provides measurements in the initial part of the propagation (approximately ten minutes after t_0) effectively constraining the initial part of the propagation. Meanwhile Svalbard, being the last station performing observations, anchors the trajectory in its final edge reducing the accumulated propagation errors and assisting the filter in minimizing the residuals across the entire observation period.

On the other hand, Kourou-Troll is the couple performing worst. Despite the overall good spatial coverage, replacing Svalbard with Troll (LAT = -72.01) fails to achieve the same level of accuracy as the previous combination. The reasons are to be identify in more limited geometric diversity of the observations (Troll is less polar than Svalbard), and in the timing of Troll's measurements, which occur immediately after those from Kourou, thereby limiting their temporal distribution. This reduced temporal coverage weakens the ability to constrain the trajectory over the full interval, further diminishing the precision of the estimation.

The final pair considered is Troll-Svalbard, which, as highlighted in Table 6, excels in estimating the inclination due to both stations being located at high latitudes. Their polar positions allow for measurements that are highly sensitive to variations in the inclination, making this combination particularly effective for this parameter. However, the lack of geographical diversity between the two stations limits the range of observation angles, which is critical for accurately estimating the semi-major axis. As a result, while Troll-Svalbard performs well for inclination, it struggles to achieve comparable precision for the semi-major axis.

A number of simulations were run due to the stochastic nature of the analysis. They outlined how the Kourou-Svalbard network's accuracy continuously outperformed other combinations for semi-major axis estimation. In some cases, nevertheless, Troll-Svalbard succeeded in obtaining improved inclination estimate findings.

In conclusion, the Kourou-Svalbard network was the best option within the allotted time interval since, aside from its innate accuracy, it was also reasonably priced, with a total 65,000€.

2.5 Long-Term Analysis

The final analysis focused on a realistic nominal scenario, it requires the selection of two primary ground stations and one backup station for long-term operational planning. Unlike the approach described in Section 2.4, this selection aims to prioritize the regularity of satellite passes to ensure consistent coverage over the best possible estimate of the state. The selection process was initially approached from a theoretical standpoint; the hypotheses done have been then verified through orbital propagation to assess the consistency with the reality.

For these reasons, Troll and Svalbard were selected as the primary stations. The rationale behind this choice is their polar positions, as they allow for excellent temporal coverage

for SMOS' polar orbit and high accuracy in state estimation, especially in inclination, demonstrated in Section 2.4. Their strategic locations ensure consistent and repeatable measurements, aligning well with SMOS' orbital characteristics. Moreover, the regularity of their visibility windows simplifies scheduling activities, making them the optimal choice for long-term operational planning.

On the other hand, Kourou would have been an excellent choice to introduce geometric diversity to the measurements due to its low-latitude location. However, it is not suitable as a primary station due to to the low number of passes over an extended period of time. It was selected as the backup station, though, and will only be set on when satellite passes over its location. Despite the limited number of passes, its measurements improve significantly the estimation of the semi-major axis. This setup provides a solution that is well-balanced: when its observations are available, Kourou enhances the polar stations' accuracy in critical parameters and adds geometric diversity, while the polar stations provide reliable coverage and accurate orbital parameter estimates.

To validate the hypotheses, SMOS' state was propagated using SGP4 both forward and backward starting from its reference state at t_{ref}, for a total duration of 10 hours. Although long propagation times can reduce the reliability of the results due to the accumulation of errors, the outcomes align with the initial predictions. As shown in Fig. 9, the visibility windows of Troll and Svalbard are significantly larger compared to those of Kourou, confirming the initial considerations about their superior temporal coverage. However, further analysis with more precise propagation models is necessary to fully confirm these findings.
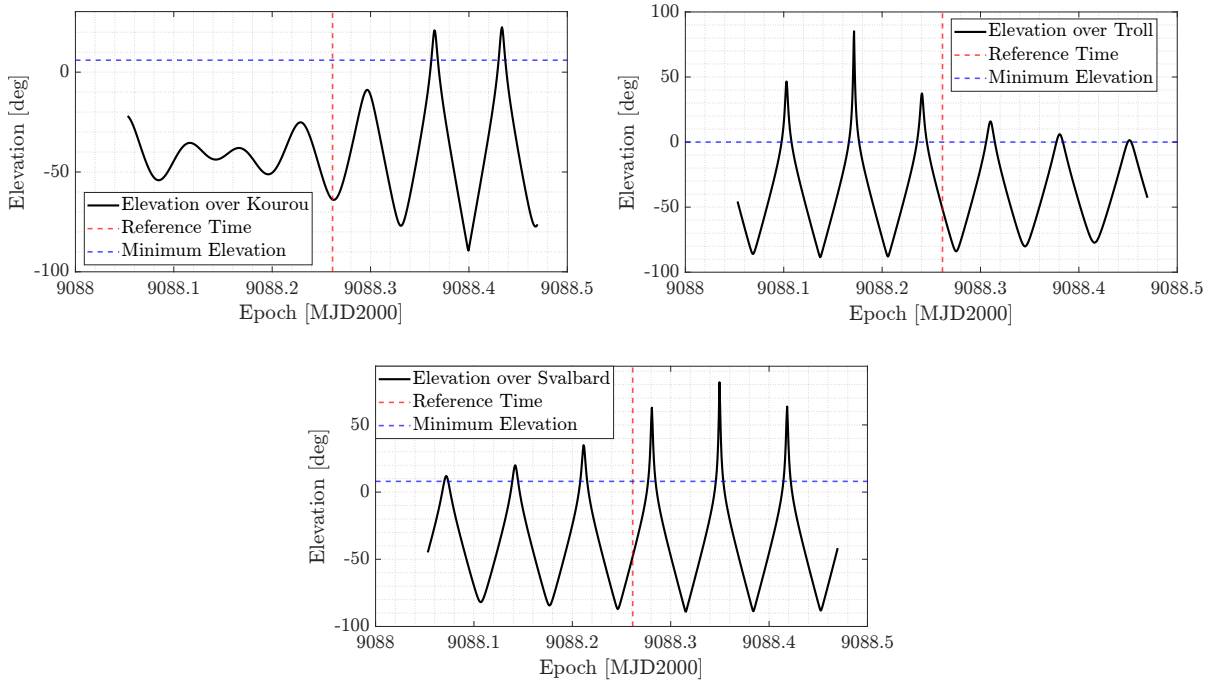

Figure 9: Elevation over time for Kourou, Troll and Svalbard: Long-term analysis

Exercise 3: Sequential filters

An increasing number of lunar exploration missions will take place in the next years, many of them aiming at reaching the Moon's surface with landers. In order to ensure efficient navigation performance for these future missions, space agencies have plans to deploy lunar constellations capable of providing positioning measurements for satellites orbiting around the Moon.

Considering a lander on the surface of the Moon, you have been asked to improve the accuracy of the estimate of its latitude and longitude (considering a fixed zero altitude). To perform such operation you can rely on the use of a lunar orbiter, which uses its Inter-Satellite Link (ISL) to acquire range measurements with the lander while orbiting around the Moon. At the same time, assuming the availability of a Lunar Navigation Service, you are also receiving measurements of the lunar orbiter inertial position vector components, such that you can also estimate the spacecraft state within the same state estimation process.
To perform the requested tasks you can refer to the following points.

1. *Check the visibility window.* Considering the initial state $\mathbf{x}_0$ and the time interval with a time-step of 30 seconds from t_0 to t_f reported in Table 8, predict the trajectory of the satellite in an inertial Moon-centered reference frame assuming Keplerian motion. Use the estimated coordinates given in Table 9 to predict the state of the lunar lander. Finally, check that the lander and the orbiter are in relative visibility for the entire time interval.

2. *Simulate measurements.* Always assuming Keplerian motion to model the lunar orbiter dynamics around the Moon, compute the time evolution of its position vector in an inertial Moon-centered reference frame and the time evolution of the relative range between the satellite and the lunar lander. Finally, simulate the measurements by adding a random error to the spacecraft position vector and to the relative range. Assume a Gaussian model to generate the random error, with noise provided in Table 8 for both the relative range and the components of the position vector. Verify (graphically) that the applied noise level is within the desired boundary.

3. *Estimate the lunar orbiter absolute state.* As a first step, you are asked to develop a sequential filter to narrow down the uncertainty on the knowledge of the lunar orbiter absolute state vector. To this aim, you can exploit the measurements of the components of its position vector computed at the previous point. Using an Unscented Kalman Filter (UKF), provide an estimate of the spacecraft state (in terms of mean and covariance) by sequentially processing the acquired measurements in chronological order. To initialize the filter in terms of initial covariance, you can refer to the first six elements of the initial covariance $\mathbf{P}_0$ reported in Table 8. For the initial state, you can perturb the actual initial state $\mathbf{x}_0$ by exploiting the MATLAB function `mvnrnd` and the previously mentioned initial covariance. We suggest to use $\alpha = 0.01$ and $\beta = 2$ for tuning the UT in this case. Plot the time evolution of the error estimate together with the 3σ of the estimated covariance for both position and velocity.

4. *Estimate the lunar lander coordinates.* To fulfill the goal of your mission, you are asked to develop a sequential filter to narrow down the uncertainty on the knowledge of the lunar lander coordinates (considering a fixed zero altitude). To this aim, you can exploit the measurements of the components of the lunar orbiter position vector together with the measurements of the relative range between the orbiter and the lander computed at the previous point. Using an UKF, provide an estimate of the spacecraft state and the lunar lander coordinates (in terms of mean and covariance) by sequentially processing the acquired measurements in chronological order. To initialize the filter in terms of initial covariance, you can refer to the initial covariance $\mathbf{P}_0$ reported in Table 8. For the initial state, you can perturb the actual initial state, composed by $\mathbf{x}_0$ and the latitude

and longitude given in Table 9, by exploiting the MATLAB function `mvnrnd` and the previously mentioned initial covariance. We suggest to use $\alpha = 0.01$ and $\beta = 2$ for tuning the UT in this case. Plot the time evolution of the error estimate together with the 3σ of the estimated covariance for both position and velocity.

Table 8: Initial conditions for the lunar orbiter.

Parameter	Value
Initial state $\mathbf{x}_0$ [km, km/s]	$\mathbf{r}_0 = [4307.844185282820, -1317.980749248651, 2109.210101634011]$
	$\mathbf{v}_0 = [-0.110997301537882, -0.509392750828585, 0.815198807994189]$
Initial time t_0 [UTC]	2024-11-18T16:30:00.000
Final time t_f [UTC]	2024-11-18T20:30:00.000
Measurements noise	$\sigma_p = 100$ m
Covariance $\mathbf{P}_0$ [km^2, km^2/s^2, rad^2]	`diag([10,1,1,0.001,0.001,0.001,0.00001,0.00001])`

Table 9: Lunar lander - initial guess coordinates and horizon mask

Lander name	MOONLANDER
Coordinates	LAT = 78°
	LON = 15°
	ALT = 0 m
Minimum elevation	0 deg

3.1   Visibility Window

The aim of the first point of Exercise 3 is to find all the data necessary to initialize the Unscented Kalman Filter (UKF) in order to improve the accuracy of the estimation of latitude and longitude of a lunar lander.

The analysis started by predicting the orbiter trajectory using a Keplerian Propagator and the initial state $\mathbf{x_0}$ provided in Table 8. The propagation, performed over the specified time interval, provided a reference trajectory, in Moon Centered Inertial (MCI), which serves as the basis to retrieve the required lander measurements. The resulting orbit is shown in Fig. 10.
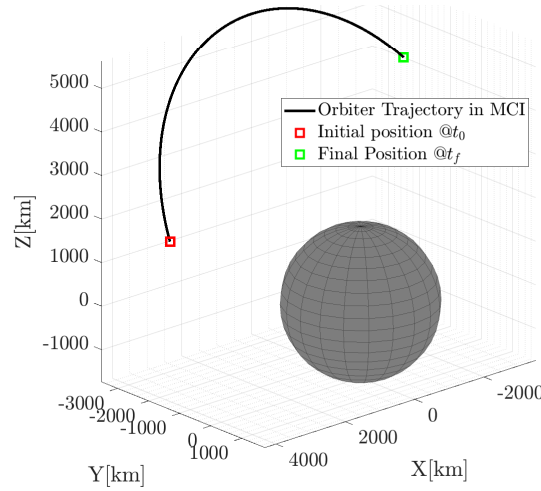

Figure 10: Orbiter Trajectory from t_0 to t_f (@Moon MCI frame).

A first guess of the lander's state in Moon Centered Moon Fixed (MCMF) reference frame was recovered (Table 10), starting from the latitudinal coordinates provided in Table 9, by exploiting the function cspice_latrec and setting to zero the velocity components. In order to define the initial state of the lander in the same reference frame as the orbiter, a rotation from MCMF to MCI was performed through cspice_sxform.

x [km]	y [km]	z [km]	v_x [km/s]	v_y [km/s]	v_z [km/s]
348.917	93.492	1699.434	0	0	0

Table 10: Lunar Lander State at t_0 (@Moon MCMF reference frame).

In order to ensure coverage between lander and orbiter throughout the time interval, their relative position was computed and rotated in the lander's TOPOCENTRIC reference frame. From this Range, Azimuth, and Elevation were derived through cspice_xfmsta, with the Elevation being critically assessed to ensure it remained above the minimum operational threshold. Fig. 11 confirms that orbiter and lander maintained continuous relative visibility during the entire time interval.
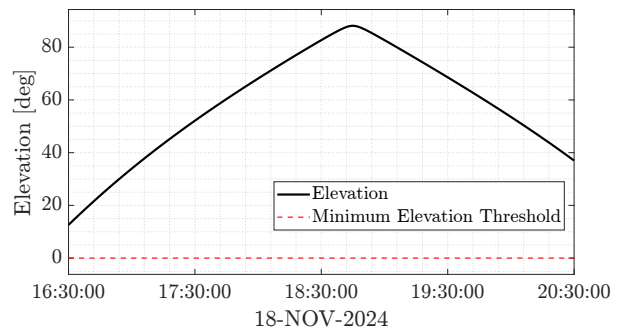

Figure 11: Relative Elevation over time

3.2   Measurements Simulation

Moving forward to reduce the uncertainties on the estimate of the lander latitude and longitude, this section focuses on the simulation of the measurements needed for the purpose. As stated in Section 3, the orbiter acquires range measurements of the lander while its inertial position is tracked by a Lunar Navigation Service. For the simulation, the orbiter position was computed following the procedure described in Section 3.1. The range measurements were recovered similarly to Section 3.1 but exploiting the provided kernel and the `cspice_spkezr` function to retrieve the state of the lander in MCI.

This process produces nominal measurements without added noise, showcasing the time evolution of the simulated quantities, as illustrated in Fig. 12.
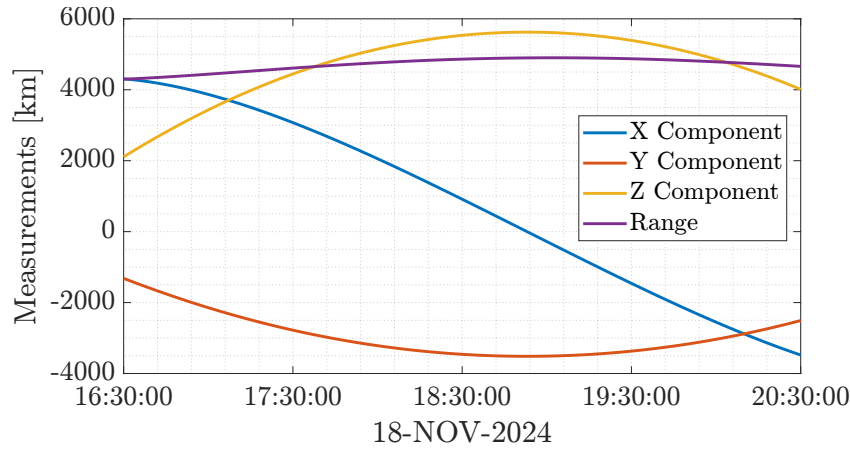

Figure 12: Time Evolution of the Nominal Measurements

Subsequently, to simulate a real-world scenario, noise was added to each measurement using a multivariate Gaussian distribution generated with the MATLAB function `mvnrnd`, employing the standard deviation of the noise provided in Table 8. After adding the noise, the difference between the noisy and nominal measurements was plotted alongside the corresponding 3σ bounds to validate that the added noise adhered to the desired level. The results, shown in Fig. 13, demonstrate that all quantities remain within the defined bounds, confirming that the added noise follows the expected Gaussian distribution.
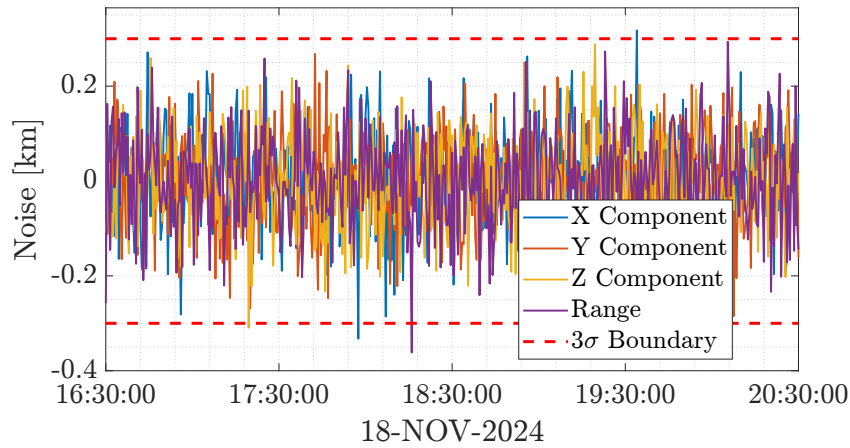

Figure 13: Noise applied to the measurements and 3σ bounds

3.3 Lunar Orbiter State Estimation

The first step of the estimation process involved the implementation of an Unscented Kalman Filter (UKF) to reduce the uncertainty in the state estimation of the lunar orbiter. For this purpose, only the position components provided by the Lunar Navigation Service were utilized as measurements.

The filter was initialized exploiting the MATLAB function `mvnrnd`, based on the initial state $\mathbf{x_0}$ and covariance $\mathbf{P_0}$ reported in Table 8. The UKF operates by propagating a set of sigma points $(\boldsymbol{\chi_i})$ generated from the current state estimate and covariance, through the keplerian dynamics. At each time step, it utilized the propagated sigma points and the real measurements to compute the a priori estimate and covariance alorng with the Kalman Gain. These are then exploited to update the a posteriori estimate and covariance. The workflow of the generic timestep of the filter is detailed in Algorithm 1.

Algorithm 1 General UKF scheme for step $t_{k-1} \rightarrow t_k$

1: **Given:** A posteriori estimate $\mathbf{x}_{k-1}$ and covariance $\mathbf{P}_{k-1}$ at t_{k-1} and measurements $\mathbf{y_k}$, $\mathbf{R_k}$ at t_k
2: **Integration Step:**
3: Generate sigma points $\boldsymbol{\chi_{k-1}}$ from $\hat{\mathbf{x}}_{k-1}^+$ and $\mathbf{P}_{k-1}^+$
4: Propagate with Keplerian dynamics. **Output:** $\boldsymbol{\chi_k}$
5: **Prediction Step:**
6: Compute a priori estimate: $\hat{\mathbf{x}}_k^- = \sum \mathbf{W_i}^{(m)} \boldsymbol{\chi_k}$
7: Compute a priori covariance: $\mathbf{P}_k^- = \sum \mathbf{W_i}^{(c)} (\boldsymbol{\chi_k} - \hat{\mathbf{x}}_k^-)(\boldsymbol{\chi_k} - \hat{\mathbf{x}}_k^-)^\top$
8: Compute sigma points in measurement space: $\boldsymbol{\gamma_k} = \mathbf{h}(\boldsymbol{\chi_k})$
9: Compute predicted measurement mean: $\hat{\mathbf{y}}_k = \sum \mathbf{W_i}^{(m)} \boldsymbol{\gamma_k}$
10: **Update Step:**
11: Compute measurement covariance: $\mathbf{P}_{yy,k} = \sum \mathbf{W_i}^{(c)} (\boldsymbol{\gamma_k} - \hat{\mathbf{y}}_k)(\boldsymbol{\gamma_k} - \hat{\mathbf{y}}_k)^\top + \mathbf{R}$
12: Compute cross-covariance: $\mathbf{P}_{xy,k} = \sum \mathbf{W_i}^{(c)} (\boldsymbol{\chi_k} - \hat{\mathbf{x}}_k^-)(\boldsymbol{\gamma_k} - \hat{\mathbf{y}}_k)^\top$
13: Compute Kalman gain: $\mathbf{K}_k = \mathbf{P}_{xy,k} \mathbf{P}_{yy,k}^{-1}$
14: Update state: $\hat{\mathbf{x}}_k^+ = \hat{\mathbf{x}}_k^- + \mathbf{K}_k(\mathbf{y}_k - \hat{\mathbf{y}}_k)$
15: Update covariance: $\mathbf{P}_k^+ = \mathbf{P}_k^- - \mathbf{K}_k \mathbf{P}_{yy,k} \mathbf{K}_k^\top$
16: **Output:** A posteriori estimate $\mathbf{x}_k^+$, and covariance $\mathbf{P}_k^+$ at time t_k

---

Since the UKF is a sequential filter, the state estimates of the orbiter are computed iteratively at each time step from $t_0 \rightarrow t_f$. The resulting mean state vector and covariance matrix estimated by the filter at t_f are presented in Table 11 and Table 12.

Table 11: Final estimated state of the Lunar Orbiter at t_f (@Moon MCI frame).

$\mathbf{x}_f^+$	$\mathbf{r}_f = [-3479.0351, -2506.2035, 4010.7457]$
[km, km/s]	$\mathbf{v}_f = [-0.450124, 0.348539, -0.557782]$

$$\mathbf{P_f^+} = \begin{bmatrix} 7.2199e-05 & 6.7327e-06 & -1.0784e-05 & 5.7014e-09 & 3.5759e-09 & -5.7249e-09 \\ 6.7327e-06 & 8.1549e-05 & -2.8310e-05 & 5.2677e-09 & 8.8859e-09 & -9.4502e-09 \\ -1.0784e-05 & -2.8310e-05 & 1.0913e-04 & -8.4275e-09 & -9.4493e-09 & 1.8099e-08 \\ 5.7014e-09 & 5.2677e-09 & -8.4275e-09 & 1.9656e-12 & 1.2250e-12 & -1.9601e-12 \\ 3.5759e-09 & 8.8859e-09 & -9.4493e-09 & 1.2250e-12 & 1.9615e-12 & -1.8769e-12 \\ -5.7249e-09 & -9.4502e-09 & 1.8099e-08 & -1.9601e-12 & -1.8769e-12 & 3.7917e-12 \end{bmatrix}$$

Table 12: Final covariance matrix of the Lunar Orbiter State at t_f. Units: $\left[km^2, \dfrac{km^2}{s} \right]$

In order to evaluate the accuracy of the analysis in estimating the orbiter's position and velocity, two errors were defined as:

$$\text{err}_\mathbf{r} = ||\mathbf{r}_{\text{true}} - \hat{\mathbf{r}}^+|| \quad \text{err}_\mathbf{v} = ||\mathbf{v}_{\text{true}} - \hat{\mathbf{v}}^+|| \tag{6}$$

where $\mathbf{r}_{\text{true}}$ and $\mathbf{v}_{\text{true}}$ are the propagated true position and velocity vectors, respectively, and $\hat{\mathbf{r}}^+$ and $\hat{\mathbf{v}}^+$ are the corresponding estimated vectors at each time step.

The traces of the position and velocity covariance submatrices were used to calculate the standard deviations of the two values. Throughout the whole time period, the position and velocity errors continuously stay within the 3σ boundaries, as illustrated in Fig. 14. This highlights the reliability of the estimation process and confirms that the uncertainties are properly characterized by the covariance matrix. Furthermore, the substantial decrease in the initial errors for both position and velocity during the time interval demonstrates the effectiveness of the implemented filter. This rapid convergence towards smaller error magnitudes demonstrates the filter's ability to effectively handle noise-damaged measurements and improve state estimates by utilizing the Kalman gain to reduce uncertainties.
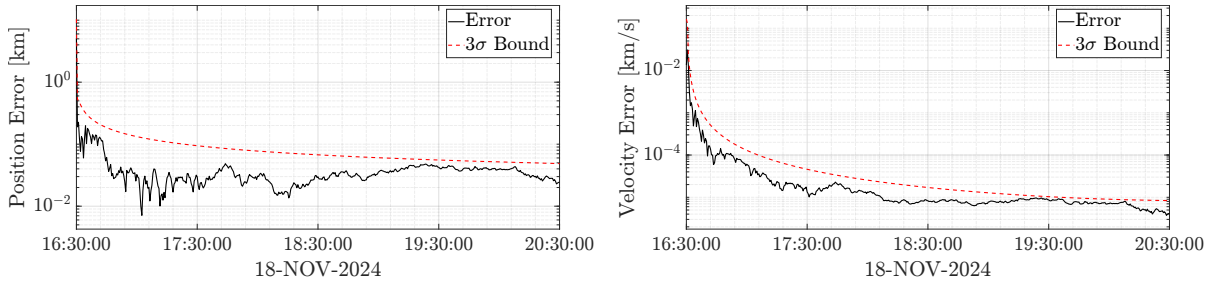

Figure 14: Evolution of the Lunar Orbiter's position and velocity errors.

3.4 Lunar Lander Coordinates Estimation

Finally, to fulfill the goal of the analysis, an UKF has been implemented considering, apart from the position measurements from Earth, even the range between orbiter and lander measurements.

The methodology employed was very similar to the one outlined in Section 3.3 with only slight modifications to enable the filter to estimate lander's coordinates. Specifically, the state vector included a concatenation of the state components of the orbiter and the latitude and longitude of the lander, initialized based on their first estimate provided in Table 9. Furthermore, Step 8 in Algorithm 1 included also the computation, through the sigma points, of the relative range at each time step. For the detailed procedure of range measurements computation, refer to Section 3.1.

Building on these premises, the output of the UKF is now an augmented state vector estimate of dimension $[8 \times 1]$, where the first six components correspond to the orbiter's state in MCI frame, and the remaining two represent the lander's coordinates on the lunar surface. The resulting mean state vector and covariance matrix estimated by the filter at tf are presented in Table 13 and Table 14.

Table 13: Final estimate at t_f of Orbiter state (@Moon MCI frame) and Lander coordinates.

Estimated state $\mathbf{x_f}$ [km, km/s, deg, deg]	$\mathbf{r}_f = [\text{-3479.0432, -2506.2011, 4010.7420}]$
	$\mathbf{v}_f = [\text{-0.4501226, 0.348540, -0.557782}]$
	$lat_f = 78.2383$
	$lon_f = 15.4167$

$$\mathbf{P}_f^+ = \begin{bmatrix} 6.3451e-05 & 3.4945e-06 & -5.6708e-06 & 3.5429e-09 & 2.5329e-09 & -4.0509e-09 & -2.5061e-07 & -2.5828e-07 \\ 3.4945e-06 & 8.1948e-05 & -2.8947e-05 & 5.2031e-09 & 8.8738e-09 & -9.4322e-09 & -2.8838e-07 & -2.5116e-07 \\ -5.6708e-06 & -2.8947e-05 & 1.1015e-04 & -8.3289e-09 & -9.4316e-09 & 1.8073e-08 & 4.5910e-07 & 4.0470e-07 \\ 3.5429e-09 & 5.2031e-09 & -8.3289e-09 & 1.7679e-12 & 1.1393e-12 & -1.8234e-12 & -5.3761e-11 & -6.0322e-11 \\ 2.5329e-09 & 8.8738e-09 & -9.4316e-09 & 1.1393e-12 & 1.9245e-12 & -1.8179e-12 & -5.2578e-11 & -4.4539e-11 \\ -4.0509e-09 & -9.4322e-09 & 1.8073e-08 & -1.8234e-12 & -1.8179e-12 & 3.6977e-12 & 8.3521e-11 & 7.0249e-11 \\ -2.5061e-07 & -2.8838e-07 & 4.5910e-07 & -5.3761e-11 & -5.2578e-11 & 8.3521e-11 & 1.0216e-08 & 1.1259e-08 \\ -2.5828e-07 & -2.5116e-07 & 4.0470e-07 & -6.0322e-11 & -4.4539e-11 & 7.0249e-11 & 1.1259e-08 & 1.3372e-08 \end{bmatrix}$$

Table 14: Covariance matrix at t_f. Units: $\left[km^2, \dfrac{km^2}{s}, rad^2 \right]$

The same validation process described in Section 3.3 was applied to this second filter. The errors for latitude and longitude were computed as the difference between filter's output and the reference values provided in the Moonlander kernel. Fig. 15 showcases the time evolution of the errors along with the corresponding 3σ boundaries for each quantity.
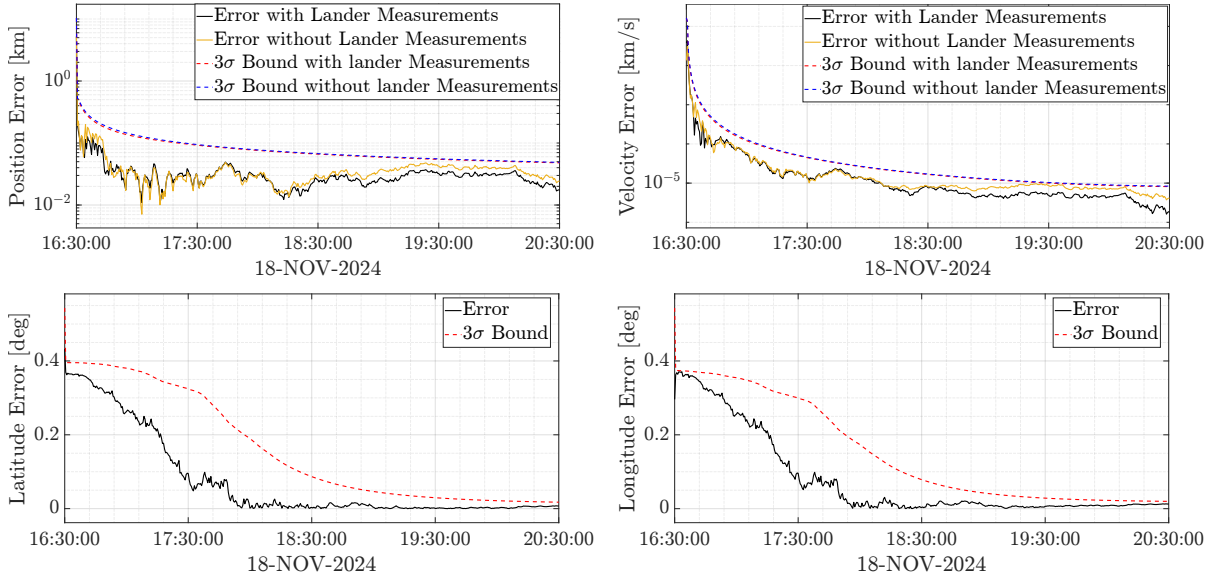

Figure 15: Evolution of Orbiter's position and velocity and Lander's Coordinates errors

As illustrated in Fig. 15, the behavior of all the errors aligns with expectations, showing a decreasing trend over time and remaining within the 3σ bounds. Therefore, the performance of the UKF can be deemed satisfactory.

Furthermore, the plots reveal that this second filter version delivers consistently more accurate results in estimating orbiter's state and covariance compared to the previous version. This improvement arises from the range measurements inclusion, which relate directly the orbiter's position to the lander's coordinates, thereby introducing additional constraints that enhance the estimation process.

Regarding the errors of the lander's coordinates, it can be noticed that, while both exhibit a decreasing trend, the convergence is much slower compared to the errors associated with the orbiter's state. This is likely due to the limited direct observability of the lander's coordinates, as they rely on indirect measurements rather than direct observations. Additionally, the non linearities in the relationship between the lander's coordinates and the measured range further contribute to the slower reduction in errors. Additionally, since the simulation was performed multiple times, some scenarios were observed in which the coordinates errors exceeded the 3σ bound. These occurrences highlight to certain limitations on the filter in estimating correctly the lander's coordinates. However, they don't undermine the overall validity of the UKF, which consistently has proven robustness and reliability.